

Article

Analysis of the Fracture Characteristics and Crack Propagation Mechanism of Fractured Sandstone under Dynamic Loading

Qi Ping ^{1,2,3,*}  and Xiangyang Li ^{1,2,3}

¹ State Key Laboratory of Mining Response and Disaster Prevention and Control in Deep Coal Mine, Anhui University of Science and Technology, Huainan 232001, China; 2021200370@aust.edu.cn

² Engineering Research Center of Mine Underground Projects, Ministry of Education, Anhui University of Science and Technology, Huainan 232001, China

³ School of Civil Engineering and Architecture, Anhui University of Science and Technology, Huainan 232001, China

* Correspondence: qping@aust.edu.cn; Tel.: +86-13956459398

Featured Application: This article may be applied to the excavation and support of coal mine roadways.

Abstract: In order to study the impact of fracture thickness on the dynamic mechanical properties of rock specimens, impact compression tests on prefabricated sandstone specimens with different fracture thicknesses and intact specimens were carried out by using a split Hopkinson pressure bar (SHPB) test device, and the dynamic mechanical parameters of the fractured sandstone specimens were obtained. The results showed that the dynamic stress–strain curves of the prefabricated fractured sandstone specimens are similar to those of the intact sandstone specimens, which can be divided into three stages: elasticity, plasticity, and failure. With the increase in the thickness of prefabricated cracks, the dynamic compressive strength of the sandstone specimens decreases in a quadratic function, the dynamic strain decreases in a power exponential function, and the dynamic elastic modulus decreases linearly. Attempts were made to quantitatively analyze the crushing degree of sandstone specimens. The average particle size of the crushed specimens was negatively correlated with the thickness of prefabricated cracks, and the fractal dimension was linearly negatively correlated with the dynamic compressive strength. The 1.5–2.5 mm prefabricated fractured sandstone specimens produced airfoil cracks and secondary cracks; the 3–3.5 mm prefabricated fractured specimens produced airfoil cracks, coplanar secondary cracks, and secondary oblique cracks; and the complete specimens were subjected to axial failure to produce axial cracks.

Keywords: rock dynamics; fractured sandstone; impact compression; crack growth; SHPB (split Hopkinson pressure bar)



Citation: Ping, Q.; Li, X. Analysis of the Fracture Characteristics and Crack Propagation Mechanism of Fractured Sandstone under Dynamic Loading. *Appl. Sci.* **2024**, *14*, 2042. <https://doi.org/10.3390/app14052042>

Academic Editor: Stefano Invernizzi

Received: 16 January 2024

Revised: 23 February 2024

Accepted: 26 February 2024

Published: 29 February 2024



Copyright: © 2024 by the authors. Licensee MDPI, Basel, Switzerland. This article is an open access article distributed under the terms and conditions of the Creative Commons Attribution (CC BY) license (<https://creativecommons.org/licenses/by/4.0/>).

1. Introduction

The size, relative spatial position, and quantity of joints in rock masses determine their damage, mechanical properties, and failure modes, often resulting in significant differences. Therefore, the problems encountered in actual construction excavation and engineering construction also vary; the presence of fissures and joints increases the uncertainty of rock engineering and makes it difficult to carry out a project. Meanwhile, the expansion and connection of internal cracks and joints are often the cause of instability and failure in many geotechnical engineering projects, and the instability of cracks leads to safety issues in practical engineering. Therefore, studying the mechanical properties and spreading mechanism of fractured rock masses is necessary.

The SHPB is a common tool used for the study of the dynamic mechanical properties of rock. The dynamic properties of intact rock have been extensively studied by scientists using the SHPB. Gao et al. [1] studied the dynamic mechanical properties of a slope rock under three conditions of drying in a normal temperature, water saturation in a normal

temperature, and low-temperature freezing. It was found that the cold shrinkage of a rock matrix is the main reason for the increase in rock strength, which provides a theoretical basis for resource exploitation and engineering construction in seasonally and permanently frozen areas in China. Li et al. [2] carried out impact tests on limestone, dolomite, and sandstone. Ping et al. [3–7] conducted impact compression tests on different types of sandstone under high-temperature and different HP conditions to study their mechanical properties and analyze their stress balance. Wang et al. [8] investigated the variation in the acoustic energy of granite under combined dynamic and static loading; they found that the law of acoustic emission energy presents two distinct characteristics. Yang et al. [9] studied the compression deformation law of ring specimens under impact compression by using numerical simulation and found that the dynamic and static deformation trends were basically the same, but there was still a gap; inertia played a major role, and the strain rate played a secondary role.

In an actual situation, there are small cracks in natural rock, and at the same time, it will become damaged during coal mine excavation and external pressure; compared to that of an intact specimen, the dynamic performance of a fractured rock mass is sensitive, resulting in cracks. Wang et al. [10] verified the mechanical properties of a 3D-printed complex fractured rock mass. Xu et al. [11] performed uniaxial compression tests on numerical models of rock masses and analyzed the effect of varying dip angles on their mechanical properties. Li et al. [12] discussed the dynamic mechanical properties of fractured specimens using different loading methods. Han et al. [13] conducted a uniaxial compression test on marble specimens with two cracks at the end, and they investigated the effect of the crack length and dip angle on the mechanical properties of marble. Tang et al. [14] discovered that confining pressure considerably strengthens sandstone samples. Wu et al. [15] found that the axial strain and circumferential strain of fractured rock specimens reduced with more prefabricated cracks. Wang et al. [16] conducted SHPB loading and uniaxial compression tests on rock-like samples with different inclination angles. Their study revealed that the specimen's peak strength was at its lowest when the crack dip angle was 45° , and the crack initiation angle reduced gradually as the crack dip angle increased. Zhu et al. [17] carried out the numerical simulation of a rock with a central crack under uniaxial compression, which revealed its failure mechanism. Zhang et al. [18,19] abstracted the deformation process in the shear localization zone of fractured rock-like materials into two stages and then studied the influence of fissure space position on its penetration mechanism. Pu et al. [20] investigated the impact of the fracture angle and distribution density on the failure of multi fractured rock materials; their findings provide insight into the change in the strength of multi fractured rock in underground engineering. Zhao et al. [21] conducted SHPB loading tests on sandstone with different numbers and depths of nonpersistent fissures and analyzed their dynamic failure characteristics. Liu et al. [22] conducted one-dimensional impact tests on fractured and nonfractured rock specimens using an SHPB with a confining pressure chamber. The effects of confining pressure, filling material, and thickness on the stress waves were analyzed. Wang et al. [23] analyzed the connection between media dynamic parameters and initial gas pressure under cyclic shock. Zhang et al. [24] used cement mortar to simulate rock specimens with different angles of cracks and used an SHPB device to carry out dynamic and static loading tests, respectively. Tian et al. [25] performed uniaxial compression tests using an SHPB on 3D-printed rocks with prefabricated cracks of different inclinations. Xie et al. [26,27] investigated the energy mechanism of rock during deformation and failure. Liu et al. [28] ran SHPB tests on jointed rock masses under seven different working conditions; they studied the relationship between their dynamic strength and joints. Che et al. [29] analyzed the effect of crack angle on the specimen's failure strength and identified the reasons for this, which underpinned the theory of practical engineering. Wong et al. [30] investigated the mechanism of the coalescence of three parallel cracks in rock-like materials. Martin [31] divided the cracks generated around the porous rock into three basic forms through experimental research: remote, primary, and shear cracks. E. J. Dzik et al. [32] conducted a systematic study on

the mode of crack propagation in holed granite under compression. McClintock et al. [33] proposed that there is a critical compressive stress that causes an open crack to close. Bobet et al. [34] used a gypsum model to prefabricate cracks and carried out uniaxial and biaxial loadings under different confining pressures. Afolagboye [35] highlighted the influence of the crack length and angle on both crack initiation behavior and propagation in a uniaxial compression test of a cracked rock model. In addition, many scholars [36–38] have analyzed different aspects of crack propagation in rock specimens under varying conditions and have made great achievements.

Based on the above research, discussions about fractured rock mass mainly focus on the impact of the change in fracture dip angle on the dynamic performance of rock, and we found that the previous studies mainly focused on the variation in the kinetic parameters of specimens with small fracture thicknesses (<1 mm) [39]. Therefore, in this study, we chose to use 0.5 mm as a gradient, and the crack thicknesses selected were within 1.5–3.5 mm. Therefore, this article describes the use of a split Hopkinson pressure bar (SHPB) tester to perform impact compression tests on intact sandstone samples with different prefabricated crack thicknesses. The variation in the dynamic performance of prefabricated fractured sandstone specimens with fractures of different thickness was explored, and this analysis focused on the mode and mechanism of crack propagation.

2. Sample Processing and Testing Equipment

2.1. Processing of the Prefabricated Fractured Sandstone Specimens

The rock samples used in this experiment were taken from sandstone on a roadway along the Pan'er Coal Mine in Huainan, Anhui Province, China. According to the Chinese Test Procedure for the Dynamic Characteristics of Rocks [40], using rock processing equipment, the rock sample was processed into a $\phi 50 \times 50$ mm cylinder through core sampling, cutting, and polishing. Prefabricated fully penetrating cracks were made along the cylindrical surface of the specimen using water jet technology. As shown in Figure 1, the angle between the prefabricated cracks and the end face of the specimen $\alpha = 45^\circ$; the length $l = 20$ mm; and the thickness $a = 1.5$ mm, 2 mm, 2.5 mm, 3 mm, and 3.5 mm. Figure 2 presents a diagram of the fractured sandstone specimens.

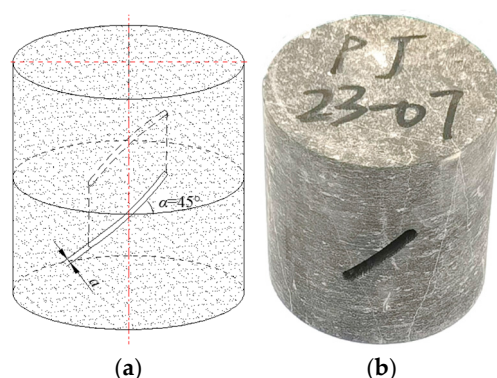


Figure 1. Location of the prefabricated cracks in sandstone specimens. (a) Schematic diagram of prefabricated cracks. (b) Sample diagram.

2.2. SHPB Testing Device

The impact compression test was conducted using an SHPB test device from the State Key Laboratory for Mining Response and Disaster Prevention and Control (as shown in Figure 3); the device consists of pressure bar and data acquisition systems. The device has a yield strength > 800 MPa, an equipment pressure rod diameter of 50 mm, an incident rod length of 2 m, and a transmission rod length of 1.5 m. An impact air pressure of 0.4 MPa was selected to test the specimens, the speed at impact was about 18 m/s, and the incident energy was about 119.54 MPa. The voltage measured using the strain gauges of both the

incident and projection bars and the dynamic mechanical parameters were calculated using the three-wave method.



Figure 2. Diagram of the fractured sandstone specimens.



Figure 3. The SHPB device.

Compression tests were conducted on intact sandstone samples and sandstone samples with different prefabricated crack thicknesses to determine their impact. Figure 4 shows the sketch of specimen clamping.

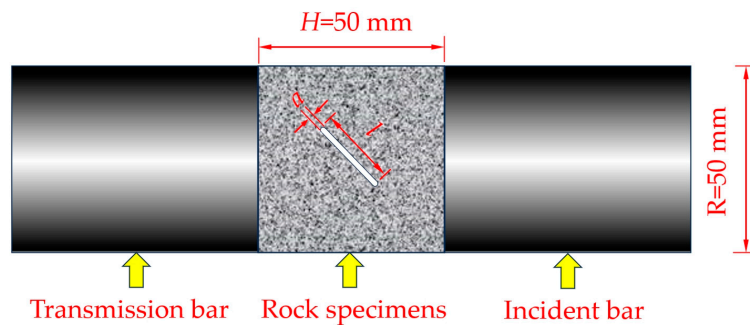


Figure 4. Sketch of specimen clamping.

Using the device, electrical signals were measured on the strain gauges, and the obtained test data were processed using the three-wave method (as shown in Equation (1) to obtain the basic dynamic parameters of the specimen).

$$\left. \begin{aligned} \sigma(t) &= \frac{E_0 A_0}{2 A_S} [\varepsilon_I(t) + \varepsilon_R(t) + \varepsilon_T(t)] \\ \varepsilon(t) &= -\frac{C_0}{L_S} \int_0^\tau [\varepsilon_I(t) + \varepsilon_R(t) - \varepsilon_T(t)] dt \\ \dot{\varepsilon}(t) &= -\frac{C_0}{L_S} [\varepsilon_I(t) + \varepsilon_R(t) - \varepsilon_T(t)] \end{aligned} \right\} \quad (1)$$

where A_0 indicates the cross-sectional area of the lever; A_S indicates the cross-sectional area of the specimen; ε_I , ε_R , and ε_T denote the incident, reflected, and transmitted strains, respectively; C_0 indicates the longitudinal wave velocity of the compression rod; τ indicates the duration of stress waves; and L_S indicates the length of the rock specimens.

3. SHPB Test Results of the Prefabricated Fractured Sandstone Specimens

The properties of rock dynamics can indicate a rock’s ability to resist deformation and damage under pressure. It is crucial to understand and master these properties to analyze and predict the behavior of rocks.

3.1. Dynamic Stress–Strain Curve of Prefabricated Fractured Sandstone Specimens

Compression tests were conducted on sandstone specimens, including intact specimens and five groups with varying prefabricated crack thicknesses; the physical and dynamic parameters of the fractured sandstone specimens are shown in Table 1.

Table 1. Dynamic parameters of fractured sandstone specimens.

Crack Thickness /mm	Test Piece Number	Volume / $\times 10^{-3}$ cm ³	Physical Parameters			Dynamic Parameters			
			Quality /g	Density /cm ³ /g	Effective Volume /cm ³	Dynamic Compressive Strength/MPa	Dynamic Strain / $\times 10^{-3}$	Dynamic Modulus of Elasticity/GPa	Average Strain Rate
0	PJ23-16	98.20	273.67	2.8	98.20	103.23	5.78	46.05	89.8
	PJ23-17	98.65	275.77	2.8	98.65	97.72	5.47	47.50	84.5
	PJ23-18	98.36	273.62	2.8	98.36	96.56	5.27	50.28	89.3
1.5	PJ23-01	98.99	272.56	2.8	97.69	84.57	4.25	38.33	86.7
	PJ23-02	98.70	270.59	2.7	97.39	91.20	3.81	30.62	91.7
	PJ23-03	99.23	268.72	2.7	97.92	87.72	4.52	36.08	86.6
2.0	PJ23-04	98.31	270.30	2.7	96.35	73.46	3.21	30.50	88.7
	PJ23-05	98.59	266.92	2.7	96.63	78.48	3.76	30.96	85.9
	PJ23-06	98.55	261.90	2.7	96.59	77.24	3.54	34.33	92.9
2.5	PJ23-07	98.78	269.84	2.7	96.33	73.96	3.28	23.51	85.1
	PJ23-08	98.88	262.79	2.7	96.43	71.58	3.48	25.43	84.7
	PJ23-09	98.69	257.02	2.6	96.24	78.14	3.58	20.19	87.3
3.0	PJ23-10	98.26	258.98	2.6	95.65	64.45	3.30	18.12	91.2
	PJ23-11	98.86	265.23	2.7	96.24	67.53	3.27	19.95	90.1
	PJ23-12	98.07	264.60	2.7	95.46	60.86	3.16	16.55	88.0
3.5	PJ23-13	98.11	264.47	2.7	95.06	58.68	2.81	13.93	93.7
	PJ23-14	98.14	259.78	2.6	95.09	50.49	2.18	12.35	86.0
	PJ23-15	98.54	264.44	2.7	95.50	61.46	2.97	11.56	93.5

From Table 1, it is clear that the discrete dynamic parameters of the specimen were relatively good. The average strain rate of the fractured sandstone specimens fluctuated slightly, but the overall change was not significant; the reason for this fluctuation in strain rate may be due to errors that occurred during the operation of the equipment. Typical dynamic stress–strain curves were drawn, as shown in Figure 5.

It can be seen from Figure 5 that the dynamic stress–strain curve of the intact sandstone specimen is located above those of the prefabricated fractured sandstone specimens, and the changes are similar, which can be divided into three stages. The first is the elastic stage. In this stage, the dynamic stress–strain curve rises linearly and obeys Hooke’s law. The

stress concentration zone at the tip of the prefabricated crack begins to crack and gradually expands. The second is the plastic stage, in which the dynamic stress–strain curve is convex. As the stress increases, the slope of the curve gradually decreases to 0. The third is the failure stage, in which the stress gradually decreases. As the crack continues to expand, the specimen gradually loses its bearing capacity until it is completely destroyed.

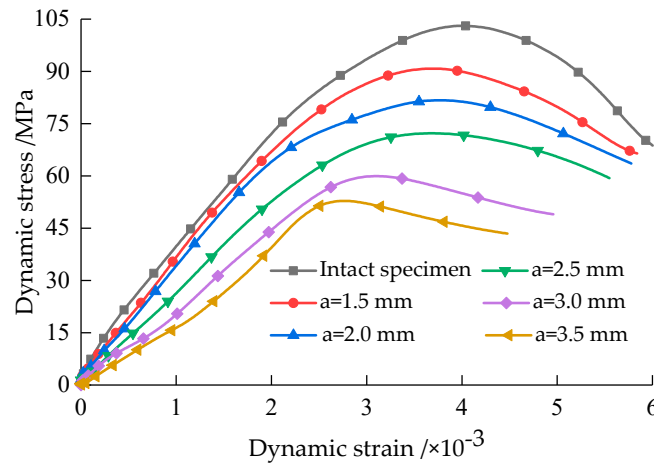


Figure 5. Dynamic stress–strain curve of the prefabricated fractured sandstone specimens.

3.2. Dynamic Mechanical Parameters of the Prefabricated Fractured Sandstone Specimens

The variation in dynamic mechanical parameters of the prefabricated fractured sandstone specimens with different fracture thicknesses is shown in Figure 6.

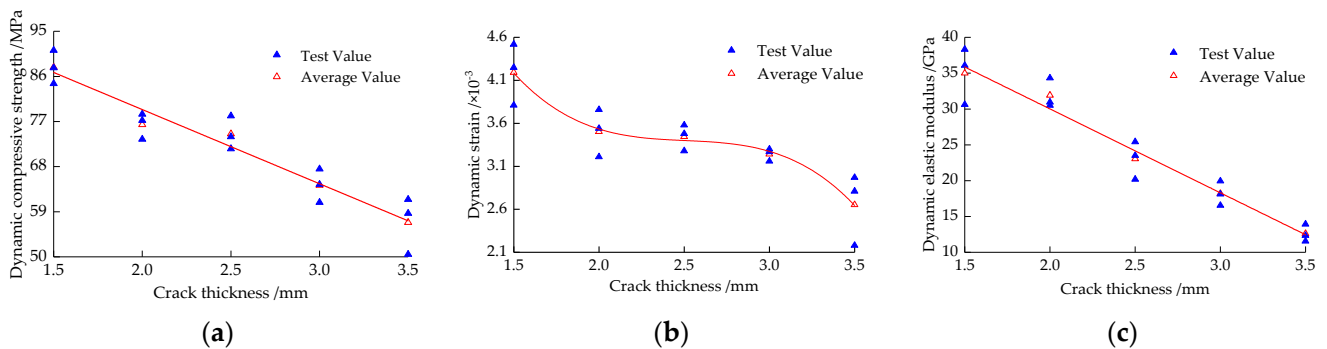


Figure 6. Dynamic mechanical parameters of the prefabricated fractured sandstone specimens varied with crack thickness. (a) Dynamic compressive strength. (b) Dynamic strain. (c) Dynamic modulus of elasticity.

From Figure 6a, the results indicate that the dynamic compressive strength of the sandstone specimens decreased as the prefabricated crack thickness increased. The dynamic compressive strength of intact sandstone specimens was 99.17 MPa, which was higher than that of the prefabricated crack specimens. Compared with the intact specimens, the dynamic compressive strength of the sandstone specimens with a prefabricated crack thickness of 1.5–3.5 mm decreased by 11.43%, 22.97%, 24.82%, 35.18%, and 42.64%, respectively. The dynamic compressive strength and thickness of the prefabricated crack showed a linear negative correlation, and the fitting function is shown in Equation (2).

$$\sigma_d = -14.804a + 108.998 \quad (R^2 = 0.970) \tag{2}$$

Compared to the specimens with larger prefabricated crack openings, cracks with smaller openings were almost closed. At this time, the normal stress acting on the surface of prefabricated cracks was greater, and the frictional resistance generated on the crack

surface also increased, thereby weakening the stress concentration at the crack tip. As the crack opening increased, the frictional resistance generated by the crack surface gradually decreased until it reached 0. The normal stress acting on the crack surface gradually transformed from frictional resistance to the driving force promoting crack propagation, resulting in a gradual decrease in the dynamic compressive strength of the specimen.

Figure 6b shows that the dynamic strain of the pre-cracked sandstone specimens decreased gradually as the pre-crack thickness increased, and this became smaller. The dynamic strain of intact sandstone specimens was 5.51×10^{-3} , and the dynamic strain of sandstone specimens with the prefabricated crack thickness of 1.5–3.5 mm was 4.19×10^{-3} , 3.50×10^{-3} , 3.45×10^{-3} , 3.24×10^{-3} , and 2.65×10^{-3} , respectively. The dynamic strain of sandstone specimens was negatively correlated with the thickness of prefabricated cracks, and the fitting relationship is shown in Equation (3).

$$\varepsilon_d = -6.80a^3 + 5.115a^2 - 12.916a + 14.346 \quad (R^2 = 0.997) \quad (3)$$

From Figure 6c, the results show that the dynamic elastic modulus of the sandstone specimens decreased as the crack thickness increased. The dynamic elastic modulus of the intact sandstone specimen was 47.94 GPa, and the dynamic elastic moduli of the sandstone specimen were 35.01, 31.93, 23.04, 18.21, and 12.61 GPa, respectively, when the prefabricated crack thickness was 1.5–3.5 mm. There was a linear negative correlation between the dynamic elastic modulus and the thickness of the prefabricated crack. The fitting function is shown in Equation (4).

$$E_d = -11.703a + 53.419 \quad (R^2 = 0.984) \quad (4)$$

When the fractured specimen is subjected to impact compression, the upper and lower surfaces of the crack first close. As the crack opens, the compressible space on the crack surface decreases. Therefore, the dynamic elastic modulus of the fractured sandstone specimen increases as the crack opens.

4. Analysis of Specimen Fragmentation

Fractal theories can be used to quantitatively describe complex objects in the physical world. This can also help to reveal damage mechanisms in rock masses. Sieve tests were analyzed in conjunction with a relevant fractal theory.

4.1. Crushed Particle Size of the Specimens

The size d_s of the crushed specimen was used to quantitatively analyze the degree of crushing after impact compression. The average crushing particle size of the specimen is shown in Equation (5).

$$d_s = \frac{\sum r_i d_i}{\sum r_i} \quad (5)$$

where d_s represents the average particle size of the specimen after crushing, d_i represents the pore size of different square hole sieves, r_i represents the different pore sizes, and d_i corresponds to the percentage of the mass of sandstone fragments retained in the pore size sieve to the total mass. The results after screening are shown in Table 2.

Figure 7 shows the relationship between the mean particle size of the broken particles and the fracture thickness of the pre-cracked sandstone specimen.

Table 2. Screening data of impact fragments for fractured specimens with different thicknesses.

Crack Thickness/mm	Size of Screen Mesh/mm									Gross Mass /g	Average Particle Size of Fragments /mm
	0	0.15	0.30	0.60	1.18	2.36	4.75	9.50	13.20		
0	0.25	0.09	0.22	0.39	0.78	3.04	7.40	22.23	237.69	272.09	12.47
1.5	0.11	0.34	1.25	1.80	1.94	8.30	13.45	23.31	218.48	268.98	11.87
2.0	0.19	0.20	1.30	2.05	2.98	9.89	13.04	20.83	209.45	259.93	11.75
2.5	0.25	0.37	0.88	1.62	2.75	7.01	25.86	17.40	204.22	260.36	11.54
3.0	0.44	0.26	0.91	1.20	2.00	16.21	22.81	18.13	201.14	263.10	11.32
3.5	0.54	0.30	1.22	1.78	2.78	16.35	26.04	27.88	194.99	271.88	11.06

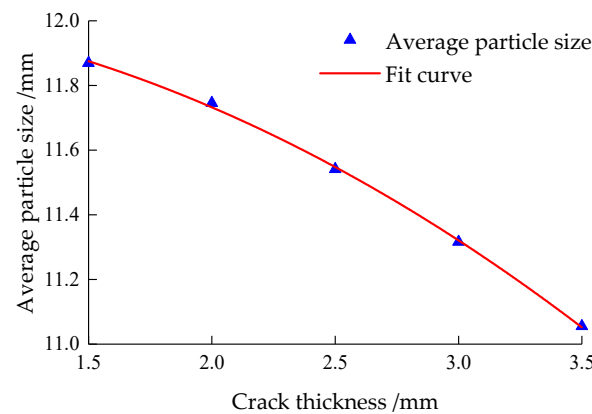
**Figure 7.** The variation in the average particle size of the specimens with prefabricated cracks.

Figure 7 shows that as the prefabricated crack thickness increased, the average particle size of the sandstone specimen after the impact failure decreased gradually. The average particle size of intact sandstone specimens was 12.47 mm. Compared with that of the intact specimens, the average particle size of the prefabricated fractured sandstone specimens was greatly reduced because the cracks weakened their ability to resist deformation. When the thickness of prefabricated cracks reached 3.5 mm, the internal force of the sandstone specimens was extremely uneven, the average particle size after crushing was the smallest, and the degree of crushing was the most obvious. The fitting relationship is shown in Equation (6).

$$d_s = -0.084a^2 + 0.010a + 12.050 \quad (R^2 = 0.998) \quad (6)$$

4.2. The Fractal Dimension of the Broken Fragments after the Specimen Had Been Broken

The fractal dimension analysis of fragments of the sandstone specimens with different prefabricated crack thicknesses after impact compression was carried out using the results of the screening test in combination with the relevant fractal theory. The fragment mass–equivalent size fractal dimension relationship is shown in Equation (7).

$$b = \frac{\lg(M_r/M)}{\lg r} \quad \text{and} \quad D = 3 - b \quad (7)$$

where b represents the slope of the linear function in the double logarithmic $\lg(M_r - M) - \lg r$ coordinate, M_r represents the corresponding fragment mass with the characteristic size r , and M represents the total mass of the sandstone specimen fragments.

The $\lg(M_r - M) - \lg r$ double logarithmic data of sandstone specimens with different prefabricated crack thicknesses were plotted and linearly fitted, as shown in Figure 8 and Table 3.

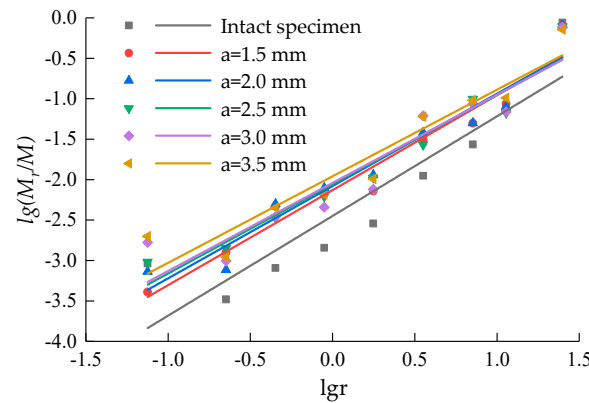


Figure 8. Linear fitting graph of $\lg(M_r/M) - \lg r$ for the fractured specimens with different thicknesses.

Table 3. Calculation results of fractal dimension of fracture specimens with different lengths.

Crack Thickness/mm	Linear Function Slope	Correlation Coefficient R ²	Fractal Dimension
0	1.2323	0.848	1.7677
1.5	1.1744	0.956	1.8256
2.0	1.1414	0.944	1.8586
2.5	1.1039	0.923	1.8961
3.0	1.0895	0.894	1.9105
3.5	1.0704	0.918	1.9296

Figure 9 shows the relationship between dynamic compressive strength and fractal dimension for the sandstone samples with different prefabricated crack thicknesses.

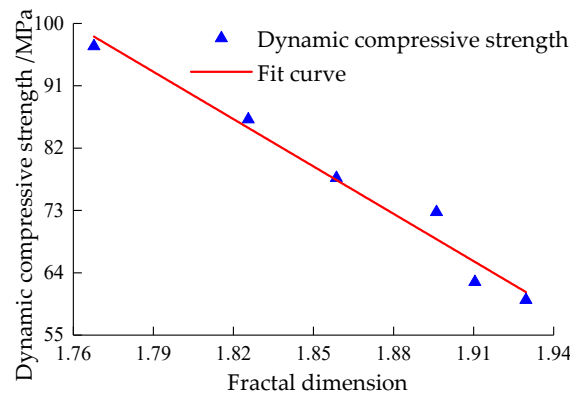


Figure 9. Relationship between dynamic compressive strength and the fractal dimension of the prefabricated fractured sandstone specimens.

It can be seen from Figure 9 that the dynamic compressive strength of the prefabricated fractured sandstone samples decreased with the increase in the fractal dimension of fragments after impact compression, showing a linear negative correlation. The fitting relationship is shown in Equation (8). The change in the thickness of the prefabricated crack led to a change in the ability of the sandstone specimen to absorb stress waves. When the dynamic compressive strength increased progressively, the ability of the specimen to resist crack extension increased gradually, and the fractal dimension decreased gradually.

$$\sigma_d = -227.842D + 500.860 \quad (R^2 = 0.963) \quad (8)$$

4.3. Crack Propagation Morphology

When a prefabricated crack specimen is subjected to impact compression, a stress concentration phenomenon occurs around the crack, resulting in tensile and compressive stress states at the end of the process, and the continuous release of the compressive stress from the stress concentration area to the surrounding area is the result of the initiation and development of the crack [21,22,41–43]. Figure 10 shows the crack propagation mode of prefabricated cracks under impact compression.

It can be seen from Figure 10 that under the condition of impact compression, the prefabricated crack propagation mainly produced airfoil cracks caused by tensile failure and secondary cracks and secondary oblique cracks caused by shear failure. According to the impact compression failure mode of prefabricated fractured sandstone specimens, the crack propagation diagram is shown (Figure 11).

Figure 11 shows that the failure modes of prefabricated fractured sandstone samples were different from those of the intact samples. The cracks affected the initiation and expansion of internal defects in the sandstone specimens.

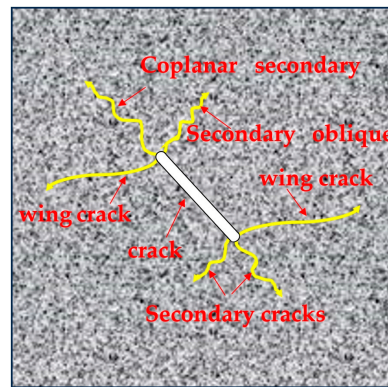


Figure 10. Prefabricated crack propagation mode.

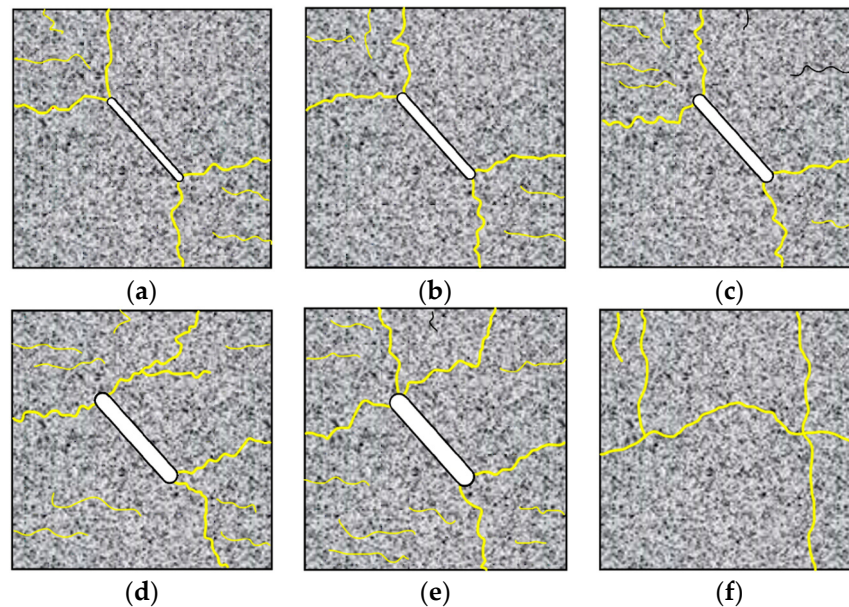


Figure 11. Specimen crack propagation mode diagram. (a) $a = 1.5$ mm. (b) $a = 2$ mm. (c) $a = 2.5$ mm. (d) $a = 3$ mm. (e) $a = 3.5$ mm. (f) Intact specimen.

The failure modes of sandstone specimens with prefabricated cracks of 1.5–2.5 mm were basically the same; the cracks initiated from the end and developed along the direction of principal stress. The rock failure surface was composed of an airfoil crack generated

at the end of the prefabricated crack and the expansion of the secondary crack. When the thickness of the prefabricated cracks reached 3 mm and 3.5 mm, the sandstone specimens began to produce coplanar secondary and secondary oblique cracks, which formed a rock failure surface with airfoil cracks. The cracks of the intact sandstone specimens were mainly tensile, and the axial cracks caused by axial tensile failure were accompanied by circumferential cracks caused by splitting failure.

4.4. Crack Propagation Mechanism

According to the sliding crack model theory and rock fracture mechanics [44,45], effective shear stress on the crack surface is described as follows:

$$\tau_{eff} = \tau - \mu\sigma_n \tag{9}$$

where τ_{eff} represents the shear stress of sliding between fracture surfaces, which is the main factor causing initiation and propagation at the crack tip; and τ , μ , and σ_n represent the shear stress, friction coefficient, and normal stress on the fracture surface, respectively.

According to the superposition principle of stress field, under the action of one-way compression, the horizontal compressive σ_x , normal compressive σ_y and shearing stresses τ_{xy} are expressed as follows:

$$\left. \begin{aligned} \sigma_x &= \sigma_1 \sin^2 \alpha \\ \sigma_y &= \sigma_1 \cos^2 \alpha \\ \tau_{xy} &= \sigma_1 \sin \alpha \cos \alpha \end{aligned} \right\} \tag{10}$$

where σ_1 represents the maximum principal stress, and α represents the angle between the prefabricated crack and the vertical direction. According to the above equation, when the inclination angle of the prefabricated crack is 45° , the stress intensity on the crack surface is the largest, and crack initiation at the tip is sufficient. By combining Formulas (9) and (10), the following equation is obtained:

$$\tau_{eff}(\alpha) = \frac{\sigma_1}{2} \sin(2\alpha) - \mu\sigma_1 \cos^2 \alpha \tag{11}$$

Under the condition that the length of the prefabricated crack is constant, the bearing capacity of the crack body is the lowest when the shear stress on its surface is the largest. By deriving the above formula with respect to the inclination angle α , which is equal to 0, we obtain the following Equation (12):

$$\alpha_0 = \frac{1}{2} \arccot(-\mu) = \frac{1}{2} (\pi - \arccot \mu) \tag{12}$$

when $\mu = 0$, crack propagation is in an ideal situation, the fracture surface closes, there is no friction, and the angle is $\alpha = 45^\circ$. This result is the same as the result of Equation (11).

According to the theory of elliptical cracking, the stress σ_θ at the boundary end of elliptical crack under uniaxial compression is given as follows:

$$\left. \begin{aligned} \sigma_\theta &= \sigma_y \frac{3+m}{1-m} - \sigma_x, \text{ at the end of the long axis} \\ \sigma_\theta &= \sigma_x \frac{3-m}{1+m} - \sigma_y, \text{ at the end of the minor axis} \end{aligned} \right\} \tag{13}$$

where $m = (c - b)/(c + b)$. The long axis of the crack is given by $2c$ and the short axis is given by $2b$. By substituting Equation (10) into the above equation, we obtain the Equation (14):

$$\left. \begin{aligned} \sigma_\theta &= \sigma_1 (\cos^2 \alpha \times \frac{3+m}{1-m} - \sin^2 \alpha), \text{ at the end of the long axis} \\ \sigma_\theta &= \sigma_1 (\sin^2 \alpha \times \frac{3-m}{1+m} - \cos^2 \alpha), \text{ at the end of the minor axis} \end{aligned} \right\} \tag{14}$$

According to the analysis of Equation (14), with the increase in the thickness of the prefabricated crack, the transverse pressure of the crack surface increases gradually, and a crack gradually initiates in the middle position. However, Figure 7 shows that there was no

tensile crack in the middle of the prefabricated crack of the sandstone specimen; the reason for this may be that with the increase in prefabricated fracture thickness, the peak strength of fractured rock mass decreases gradually although the tensile stress in the middle of the crack theoretically equates to the generation of the middle crack. However, because of the low strength of the crack, the crack surface closes quickly under the action of compressive stress, so deformation is not fully reflected, resulting in tensile stress in the middle of the prefabricated crack that does not reach the threshold value.

In summary, for the 45° prefabricated crack, shear stress in the progressive stress area is enough to drive an airfoil crack, and the failure of the crack body can be explained by the sliding crack model theory; however, this cannot be quantitatively analyzed. At this time, the existence of normal and transverse compressive stresses will affect crack propagation and the crack initiation angle.

5. Discussion

The previous studies have shown that when the fissure inclination angle is 45°, the compressive strength of the specimen is at its lowest, and the samples are more likely to be damaged. Therefore, this study selected 45° fissured sandstone for analysis. Under dynamic loading [20,45], the dynamic compressive strength of the specimen gradually decreases as the crack thickness increases. This change is similar to the rule governing the peak strength of specimen with cracks under static loading conditions. In terms of the damage pattern under static loading [16,20], the specimens mainly exhibited shear or compression shear damage caused by wing and anti-wing cracks sprouting around the cracks and penetrating along the specimen surface. Compared to this test, the change in the mechanical properties of specimens with a small crack thickness (<1 mm) [42,46] is relatively inconspicuous.

6. Conclusions

Compression tests were conducted on sandstone specimens, both intact and with prefabricated cracks of varying thicknesses, to investigate the changes in dynamic mechanical properties. The average particle size was used to quantitatively analyze the degree of fragmentation, and the crack propagation mechanism was analyzed. The main conclusions are as follows:

- (1) The dynamic stress–strain curve of prefabricated fractured sandstone samples is similar to that of intact sandstone samples. There are three stages that can be roughly divided according to the stress–strain curves of the specimens: elasticity, plasticity and failure.
- (2) With the increase in the thickness of prefabricated cracks, there is a quadratic decrease in the dynamic compressive strength of sandstone specimens, the dynamic strain decreases in a power exponential function, and the dynamic elastic modulus decreases linearly.
- (3) By increasing the thickness of the prefabricated cracks, the average particle size of the sandstone specimens decreases in a quadratic function, and the degree of fragmentation becomes increasingly obvious. As the dynamic compressive strength increases, the fractal dimension of the sandstone specimens after crushing reduces linearly.
- (4) When the sandstone specimens with a prefabricated crack thickness of 1.5–2.5 mm are impacted, airfoil and secondary cracks are generated. When the prefabricated crack thickness is 3–3.5 mm, airfoil, coplanar secondary, and secondary oblique cracks are generated. The intact sandstone specimens develop axial cracks caused by axial tensile failure.
- (5) The specimen with a 45° angle between the prefabricated crack and the loading direction possess the most ideal crack propagation condition; therefore, the stress intensity on the crack surface is the largest, and the initiation of an airfoil crack at the tip of the prefabricated crack is the most suitable. The shear stress in the crack's

progressive stress drives airfoil cracking. Crack propagation can be explained by the sliding crack model theory.

A large number of cracks will be produced by natural factors in the formation of rocks, and if we ignore the influence of other factors, including the development of internal joints, fissures, and other structural elements and their relationships, we will not be able to truly understand the nature of rock body disasters. This study can provide a certain theoretical basis for the mechanical properties of fractured rocks in the process of coal mine excavation and roadway support, and the influence of fracture geometry on the mechanical properties of rocks should be studied in the future.

Author Contributions: Conceptualization, Q.P.; software, Q.P.; validation, X.L.; formal analysis, X.L.; data curation, X.L.; writing—original draft, X.L.; writing—review and editing, Q.P. and X.L. All authors have read and agreed to the published version of the manuscript.

Funding: This study received funding from the National Natural Science Foundation of China (no. 52074005, and no. 52074006), the Anhui Natural Science Foundation (no. 1808085ME134), and the Anhui Postdoctoral Science Foundation (no. 2015B058).

Institutional Review Board Statement: Not applicable.

Informed Consent Statement: Informed consent was obtained from all subjects involved in the study.

Data Availability Statement: The data used to support the findings of this study are available from the corresponding author upon request. The data are not publicly available due to privacy.

Acknowledgments: We would like to thank the State Key Laboratory of Mine Response and Disaster, Anhui University of Science and Technology for facilitating the experimental conditions. We would also like to thank S.W.W., Y.J.X., J.H., S.J.S., and the other reviewers.

Conflicts of Interest: The authors declare no conflicts of interest. The funders had no role in the design of the study; in the collection, analyses, or interpretation of data; in the writing of the manuscript; or in the decision to publish the results.

References

- Gao, F.; Yang, G.; Xiong, X.; Zhou, K.P.; Li, C.; Li, J.L. Experimental study on the dynamic mechanical characteristics of slope rock under low-temperature conditions. *Chin. J. Eng.* **2023**, *45*, 171–181. [\[CrossRef\]](#)
- Li, X.F.; Li, H.B.; Liu, K.; Zhang, Q.B.; Zou, F.; Huang, L.X.; Zhao, J. Dynamic properties and fracture characteristics of rocks subject to impact loading. *J. Rock Mech. Eng.* **2017**, *36*, 2393–2405. [\[CrossRef\]](#)
- Ping, Q.; Wu, M.J.; Yuan, P.; Zhang, H. Experimental study on dynamic mechanical properties of high temperature sandstone under impact loads. *J. Rock Mech. Eng.* **2019**, *38*, 782–792. [\[CrossRef\]](#)
- Zhang, H.; Ping, Q.; Su, H.P. Study on dynamic compression SHPB test of limestone with different length diameter ratios. *Coal Sci. Technol.* **2018**, *46*, 38–43. [\[CrossRef\]](#)
- Ping, Q.; Gao, Q.; Wu, S.W. Study on Mechanical Properties of Ring Sandstone Specimen under Temperature and Water Coupling Dynamic Compression. *Minerals* **2023**, *13*, 119. [\[CrossRef\]](#)
- Ping, Q.; Wang, C.; Gao, Q.; Shen, K.F.; Wu, Y.L.; Wang, S.; Li, X.Y. Experimental Study on Dynamic Compression Mechanics of Sandstone after Coupled Alkali-Chemical-Dynamic Interaction. *Adv. Civ. Eng.* **2022**, *2022*, 1970591. [\[CrossRef\]](#)
- Ping, Q.; Ma, Q.Y.; Yuan, P. Prediction for stress equilibrium time in rock SHPB test. *Vib. Shock. Waves* **2013**, *32*, 55–60. [\[CrossRef\]](#)
- Wang, S.Q.; Wan, G.X.; Li, X.B. Acoustic emission experiment of rock failure under coupled static-dynamic load. *Explos. Shock. Waves* **2010**, *30*, 247–253. [\[CrossRef\]](#)
- Yang, C.; Xu, S.L.; Yi, H.S. Deformation properties of a ring under impact loading. *Vib. Shock. Waves* **2015**, *34*, 128–132+145. [\[CrossRef\]](#)
- Wang, X.Q.; Gao, F.Q.; Lou, J.F. Experimental research on model preparation of highly fractured rock mass based on 3D printing. *Chinese J. Rock Mech. Eng.* **2023**, *42* (Suppl. 2), 3913–3920. [\[CrossRef\]](#)
- Xu, Z.S.; Bian, Z.; Liu, Y.; Feng, F.; Zhao, H.B. The Influence of Combined Fractures and Its Dip Angles on the Mechanical Properties and Failure Characteristics of Rocks. *Min. Res. Dev.* **2022**, *42*, 140–145. [\[CrossRef\]](#)
- Li, D.Y.; Wan, Q.R.; Zhu, Q.Q.; Hu, C.W. Experimental study on mechanical properties and failure behavior of fractured rocks under different loading methods. *J. Min. Saf. Eng.* **2021**, *38*, 1025–1035. [\[CrossRef\]](#)
- Han, Z.Y.; Li, D.Y.; Zhu, Q.Q.; Liu, M.; Li, X.B. Uniaxial compression failure and energy dissipation of marble specimens with flaws at the end surface. *Chin. J. Eng.* **2020**, *42*, 1588–1596. [\[CrossRef\]](#)
- Tang, J.; Yang, S.; Elsworth, D. Three-Dimensional Numerical Modeling of Grain-Scale Mechanical Behavior of Sandstone Containing an Inclined Rough Joint. *Rock Mech. Rock Eng.* **2020**, *54*, 905–919. [\[CrossRef\]](#)

15. Wu, J.Y.; Feng, M.M.; Yu, B.Y.; Han, G.S. The length of pre-existing fissures effects on the mechanical properties of cracked red sandstone and strength design in engineering. *Ultrasonics* **2018**, *82*, 188–199. [[CrossRef](#)]
16. Wang, W.H.; Li, K.; Wang, X.J.; Jiang, H.T.; Yan, Z. Experimental study of mechanical properties of rocklike specimens containing single cracks of different inclination angles under SHPB loading. *Technol. Rev.* **2016**, *34*, 246–250. [[CrossRef](#)]
17. Zhu, W.C.; Huang, Z.P.; Tang, C.N.; Pang, M.Z. Numerical simulation on failure process of pre-cracked Brazilian disk specimen of rock. *Rock Soil Mech.* **2004**, *25*, 1609–1612. [[CrossRef](#)]
18. Zhang, P.; Li, N.; He, R.L. Research on Localized Progressive Damage Model for Fractured Rocklike Materials. *Chin. J. Rock Mech. Eng.* **2006**, *25*, 2043–2050. [[CrossRef](#)]
19. Zhang, P.; Li, N.; He, R.L.; Xu, J.G. Mechanism of Fracture Coalescence between Two Pre-existing Flaws under Dynamic Loading. *Chin. J. Rock Mech. Eng.* **2006**, *25*, 1210–1217. [[CrossRef](#)]
20. Pu, C.Z.; Cao, C.; Zhao, Y.L.; Zhang, X.Y.; Yi, Y.L.; Liu, Y.K. Numerical analysis and strength experiment of rock-like materials with multi-fissures under uniaxial compression. *Rock Soil Mech.* **2010**, *31*, 3661–3666. [[CrossRef](#)]
21. Zhao, G.Y.; Li, Z.Y.; Wu, H.E.; Wang, J.; Liu, L.L. Dynamic failure characteristics of sandstone with non-penetrating cracks. *Rock Soil Mech.* **2019**, *40* (Suppl. 1), 73–81. [[CrossRef](#)]
22. Liu, X.; Xu, H.F.; Fan, P.X.; Geng, H.S.; Mo, J.Q.; Wang, D.R. Experimental study on the stress wave attenuation effect of filled cracks in rocks under confining pressure. *Rock Soil Mech.* **2021**, *42*, 2099–2108. [[CrossRef](#)]
23. Wang, L.; Wang, A.C.; Chen, L.P.; Li, S.B.; Liu, H.Q. Dynamic characteristics and crack propagation characteristics of gas-bearing coal under cyclic impact. *Chin. J. Rock Mech. Eng.* **2023**, *42*, 2628–2642. [[CrossRef](#)]
24. Zhang, W.; Zhou, G.Q.; Zhang, H.B.; Zhang, Y. Experimental Research on the Influence of Obliquity on the Mechanical Characteristics of a Fractured Rock Mass. *J. China Univ. Min. Technol.* **2009**, *38*, 30–33. [[CrossRef](#)]
25. Tian, W.; Yu, C.; Wang, X.H.; Wu, P.F. A preliminary research on dynamic mechanical properties and energy dissipation rule of 3D printed fractured rock. *Chin. J. Rock Mech. Eng.* **2022**, *41*, 446–456. [[CrossRef](#)]
26. Xie, H.P.; Ju, Y.L.; Li, Y.; Peng, R.D. Energy mechanism of rock deformation and failure process. *Chin. J. Rock Mech. Eng.* **2008**, *09*, 1729–1740. [[CrossRef](#)]
27. Xie, H.P.; Peng, R.D.; Ju, Y. Energy dissipation of rock deformation and failure. *Chin. J. Rock Mech. Eng.* **2004**, *21*, 3565–3570. [[CrossRef](#)]
28. Liu, H.Y.; Deng, Z.D.; Wang, X.S.; Zhang, J.H.; Zhang, L.M. Similar material test study of dynamic failure of jointed rock mass with SHPB. *Rock Soil Mech.* **2014**, *35*, 659–665. [[CrossRef](#)]
29. Che, F.X.; Li, L.Y.; Liu, D.A. Fracture experiments and finite element analysis for multi-cracks body of rock-like material. *Chin. J. Rock Mech. Eng.* **2000**, *19*, 295–298. [[CrossRef](#)]
30. Wong, R.H.C.; Chau, K.T.; Tang, C.A.; Lin, P. Analysis of crack coalescence in rock-like materials containing three flaws part I. Experimental approach. *Int. J. Rock Mech. Min. Sci.* **2001**, *38*, 909–924. [[CrossRef](#)]
31. Martin, C.D. Seventeenth canadian geotechnical colloquium: The effect of cohesion loss and stress path on brittle rock strength. *Can. Geotech. J.* **1997**, *34*, 698–725. [[CrossRef](#)]
32. Dzik, E.J.; Lajtai, E.Z. Primary fracture propagation from circular cavities loaded in compression. *Int. J. Fract.* **1996**, *79*, 49–64. [[CrossRef](#)]
33. McClintock, F.A.; Walsh, J.B. Friction on Griffith cracks in rocks under pressure. *Q. J. Mech. Appl. Math.* **1961**, *14*, 283–292. [[CrossRef](#)]
34. Bobet, A.; Einstein, H.H. Fracture coalescence in rock type materials under uniaxial and biaxial compression. *Int. J. Rock Mech. Min. Sci.* **1998**, *35*, 863–888. [[CrossRef](#)]
35. Afolagboye, L.O.; He, J.; Wang, S. Experimental study on cracking behavior of moulded gypsum containing two nonparallel overlapping flaws under uniaxial compression. *Acta Mech. Sin.* **2017**, *33*, 394–405. [[CrossRef](#)]
36. Lajtai, E.Z. A theoretical and experimental evaluation of the Griffith theory of brittle fracture. *Tectonophysics* **1971**, *11*, 129–156. [[CrossRef](#)]
37. Niya, R.S.; Selvadurai, A. Correlation of joint roughness coefficient and permeability of a fracture. *Int. J. Rock Mech. Min. Sci.* **2019**, *113*, 150–162. [[CrossRef](#)]
38. Dustin, C.; Grant, B.; Zuleima, T.K. Numerical simulations examining the relationship between wall-roughness and fluid flow in rock fractures. *Int. J. Rock Mech. Min. Sci.* **2010**, *47*, 1365–1609. [[CrossRef](#)]
39. Liu, T.; Lin, B.; Yang, W. Mechanical behavior and failure mechanism of pre-cracked specimen under uniaxial compression. *Tectonophysics* **2017**, *712–713*, 330–343. [[CrossRef](#)]
40. T/CSRME001-2019; Test Procedure for Dynamic Characteristics of Rocks. Chinese Society of Rock Mechanics and Engineering; Beijing, China, 2019.
41. Li, X.B.; Tao, Z.; Li, D.Y. Dynamic strength and fracturing behavior of single-flawed prismatic marble specimens under impact loading with a split-Hopkinson pressure bar. *Rock Mech. Rock Eng.* **2017**, *50*, 29–44. [[CrossRef](#)]
42. Zou, C.J.; Wong, L.N.Y.; Loo, J.J.; Gan, B.S. Different mechanical and cracking behaviors of single-flawed brittle gypsum specimens under dynamic and quasi-static loadings. *Eng. Geol.* **2016**, *201*, 71–84. [[CrossRef](#)]
43. Irwin, G.R.; Wells, A.A. Continuum-mechanics view of crack propagation. *Metall. Rev.* **1965**, *10*, 223–270. [[CrossRef](#)]
44. Schmidt, R.A.; Rossmannith, H.P. Basics of Rock Fracture Mechanics. In *Rock Fracture Mechanics*; International Centre for Mechanical Sciences; Rossmannith, H.P., Schmidt, R.A., Eds.; Springer: Vienna, Austria, 1983; Volume 275. [[CrossRef](#)]

45. Zeng, J.J.; Zhang, Z.J.; Pu, C.Z. Fracture Experiment and Numerical Simulation of Fractured Rock-Like Samples Influenced by Opening. *Chin. J. Undergr. Space Eng.* **2022**, *18*, 1863–1872.
46. Zhuang, X.; Chun, J.; Zhu, H. A comparative study on unfilled and filled crack propagation for rock-like brittle material. *Theor. Appl. Fract. Mech.* **2014**, *72*, 110–120. [[CrossRef](#)]

Disclaimer/Publisher’s Note: The statements, opinions and data contained in all publications are solely those of the individual author(s) and contributor(s) and not of MDPI and/or the editor(s). MDPI and/or the editor(s) disclaim responsibility for any injury to people or property resulting from any ideas, methods, instructions or products referred to in the content.